Suppression of neutral pion production in deep-inelastic scattering off nuclei with the CLAS detector

Taisiya Mineeva,[1,2,*] William K. Brooks,[1,3,4,5] K. Joo,[2] H. Hakobyan,[1,3] Jorge A. López,[6] and O. Soto[7]

[1] *Universidad Técnica Federico Santa María, Valparaíso, Chile*
[2] *University of Connecticut, Storrs, Connecticut 06269*
[3] *Centro Cientifico y Tecnológico de Valparaíso, Valparaíso, Chile*
[4] *Instituto Milenio de Física Subatómica en la Frontera de Altas Energías, Santiago, Chile*
[5] *Department of Physics and Astronomy, University of New Hampshire, Durham, NH 03824, USA*
[6] *Physikalisches Institut, Universität Heidelberg, Heidelberg, Germany*
[7] *Universidad de La Serena, La Serena, Chile*

(Dated: May 29, 2023)

We present the first three-fold differential neutral pion multiplicity ratios produced in semi-inclusive deep inelastic electron scattering on carbon, iron and lead nuclei normalized to deuterium from CLAS measurements at Jefferson Lab. We found that the neutral pion multiplicity ratio is maximally suppressed for the leading hadrons (energy transfer $z \to 1$), suppression varying from 25% on carbon up to 75% in lead. An enhancement of the multiplicity ratio at low z and high p_T^2 is observed, suggesting an interconnection between these two variables. This behavior is qualitatively similar to the previous two-fold differential measurement of charged pions by the HERMES Collaboration. However, in contrast to the published CLAS and HERMES results on charged pions, we observe the largest enhancement at high p_T^2 for lightest nucleus - carbon and the lowest enhancement for the heaviest nucleus - lead. This behavior suggests a competition between partonic multiple scattering, which causes enhancement, and hadronic inelastic scattering, which causes suppression.

INTRODUCTION

Hadron formation is one of the last frontiers of QCD. While successful models of this process exist, they only have a tenuous connection to the underlying QCD origin of the process. The long distance scales involved in hadron formation currently preclude use of perturbative methods to calculate, for example, fragmentation functions (FF), which describe how color-carrying quarks and gluons turn into color-neutral hadrons or photons. The need for use of Minkowski space at high x_{Bj} currently precludes lattice QCD calculations.

The kinematic region of lepton deep inelastic scattering at high x_{Bj}, where x_{Bj} is the fraction of the proton momentum carried by the struck quark, offers a powerfully simple interpretation compared to low x_{Bj} where quark pair production dominates [1]. In the single-photon exchange approximation, a valence quark absorbs the full energy and momentum of the virtual photon; thus, the energy transfer ($\nu = E - E'$, in the lab frame) gives the initial energy of the struck quark, neglecting intrinsic quark momentum, and neglecting Fermi momentum of the nucleon for nuclear interactions. At the same level of approximation, the initial direction of the struck quark is known from the momentum transfer of the collision, which provides a unique reference axis. For nuclear targets, this essentially creates a secondary "beam" of quarks of known energy and direction, for which the interaction with the nuclear system provides information at the femtometer distance scale.

An important experimental observable sensitive to the in-medium hadronization process - the complex process of the evolution of a struck quark into multiple hadrons - is the hadronic multiplicity ratio. It is defined as the normalized yield of hadron h produced on a heavy nuclear target A relative to a light target, e.g., deuterium D:

$$\mathrm{R_h}(\nu, \mathrm{Q^2}, \mathrm{z}, \mathrm{p_T^2}) = \frac{\mathrm{N_h^A}(\nu, \mathrm{Q^2}, \mathrm{z}, \mathrm{p_T^2})/\mathrm{N_e^A}(\nu, \mathrm{Q^2})}{\mathrm{N_h^D}(\nu, \mathrm{Q^2}, \mathrm{z}, \mathrm{p_T^2})/\mathrm{N_e^D}(\nu, \mathrm{Q^2})}. \quad (1)$$

Here N_h is the number of hadrons produced in semi-inclusive deep inelastic scattering (SIDIS) events, where, following electron scattering off the quark, the leading hadron is detected in addition to the scattered electron; N_e is the number of DIS electrons within the same inclusive kinematic bins for the numerator as for the denominator; Q^2 is the virtual photon 4-momentum transfer squared, ν is the energy transfer, z is the fractional hadron energy defined as $z = \mathrm{E}_h/\nu$, and p_T^2 is the component of the hadron momentum transverse to the virtual photon direction; the dependence on ϕ_{pq}, the azimuthal angle of the hadron with the lepton plane, was integrated over. The hadronic multiplicity ratio, reflecting modification of the FF in nuclei compared to deuterium, quantifies the extent to which hadron production is enhanced or attenuated at a given value of the kinematic variables. In the absence of any nuclear effects this observable is equal to unity.

Nuclear SIDIS experiments have been performed in fixed-target conditions in facilities such as the Stanford Linear Accelerator Center - SLAC (E665), CERN Super Proton Synchrotron - SPS (EMC), Deutsches Elektronen Synchrotron - DESY (HERMES) and Jefferson Lab (CLAS). The study of nuclear SIDIS with fully identified final state hadrons began with the HERMES pro-

gram, which published a series of papers between 2001 and 2011 [2–7], opening an era of quantitative studies of color propagation and hadron formation using nuclei as spatial analyzers. Multiplicity ratios were presented for various identified hadrons ($\pi^{\pm}$, π^0, $K^{\pm}$, p, $\bar{p}$) first as one-fold functions of ν, Q^2, z or p_T^2, and later, in the final paper of this series, as two-fold differentials for charged hadrons. The one- and two-fold meson production data off nuclei can be described with some level of success by models [8–22] using two in-medium ingredients: (1) quark energy loss and (2) interactions of forming hadrons with the nuclear medium. Most models are based on only one of these ingredients, or they add these two ingredients classically. However, one model invoking interference processes gave qualitative indications that quantum mechanical effects could also play a role [23]. The final HERMES paper of this series [7] underlines the importance of multi-differential cross sections, since charged-hadron multiplicity data displays nontrivial features that cannot be captured by a one-dimensional description, particularly for the baryons. A comprehensive review can be found in Ref. [24].

This paper presents the first multi-dimensional measurement of neutral pion multiplicity ratios in SIDIS kinematics. Neutral pions are substantially more difficult to measure than charged pions due to more limited statistics and due to the presence of combinatorial backgrounds. While having a much more limited range in Q^2 and ν, the new data set has two orders of magnitude greater integrated luminosity than that of HERMES, dramatically increasing the statistical accuracy of the measurement. This allowed us to extend one-dimensional HERMES π^0 data measured up to mass number 131 [4], to three-dimensional data with mass numbers up to 208.

EXPERIMENTAL SETUP AND DATA ANALYSIS

The data were collected during the EG2 run period in Hall B of Jefferson Lab using the CEBAF Large Acceptance Spectrometer (CLAS) [25] and a 5.014 GeV electron beam. CLAS was based on a six-fold symmetric toroidal magnet, created by six large superconducting coils that divided the spectrometer into six independently instrumented sectors. The polarity of the toroidal field was chosen such that negatively charged particles were deflected towards the beam axis. CLAS had four types of detectors: drift chambers (DC) followed by Cerenkov counters (CC), time-of-flight (TOF) scintillators, and electromagnetic shower calorimeters (EC). Photons from π^0 decay were measured in the EC at angles from about 8 to 45 degrees.

One key ingredient in reducing systematic uncertainties of the multiplicity ratios was the use of a dual-target. The target system consisted of a 2 cm liquid-deuterium cryotarget separated by 4 cm from independently insertable solid targets (see Ref. [26]). The center of the liquid target cell and the solid target were placed 30 cm and 25 cm upstream of the CLAS center, respectively, in order to increase acceptance for negatively charged particles.

Since the electron beam passed simultaneously, first through the cryotarget and then through one of the solid targets, time-dependent systematic effects were reduced. Furthermore, the close spacing of the two targets compared to the large dimensions of the CLAS detector minimized detector acceptance differences between the solid and deuterium targets.

We measured the SIDIS reaction $e + A \rightarrow e' + \pi^0 + X$, where e and e' are the incident and scattered electrons, respectively, and X is the undetected part of the hadronic final state. Since the π^0 decays almost instantaneously into two photons ($\pi^0 \rightarrow \gamma\gamma$), we selected events with one scattered electron and at least two photons. The invariant mass of the two-photon system was used to identify π^0 candidates.

The scattered electrons were selected in the following ranges: $1.0 < Q^2 < 4.1$ GeV^2, $2.2 < \nu < 4.25$ GeV and $W > 2$ GeV. We required $Q^2 > 1$ GeV^2 and $W > 2$ GeV to probe nucleon structure in the DIS regime and reduce resonance region contributions; we required $\nu < 4.25$ GeV ($y = \frac{\nu}{E} < 0.85$) to reduce the size of radiative effects. These cuts also ensure $x_{Bj} > 0.1$, so that we are probing valence quarks in the target nucleon. Detector acceptance and experimental statistics limit the π^0 kinematics to: $0.3 < z < 1.0$ and $0 < p_T^2 < 1.5$ GeV^2. The event phase space was divided into two sets of three-fold differential multiplicity ratios with: 1) a total of 108 bins in (ν, z, p_T^2) integrated over Q^2 2) a total of 54 bins in (Q^2, ν, z) integrated over p_T^2. These choices were based on the physics of interest and on the available statistics.

We selected electrons by requiring a negatively charged particle with a good track in the DC and a signal in the TOF and EC. We further required a signal in the CC with a mirror number matching the particle angle, a signal in the EC matching the particle energy (with sector- and momentum-dependent cuts on the sampling fraction), a minimum energy deposited in the layer of the EC, and a coincidence time matching between the EC and TOF signals. We eliminated regions near the detector acceptance edges with non-uniform tracking efficiency in the DC and transverse shower leakage in the EC. We used the intersection of the electron track with the plane containing the ideal beam position to determine the origin of the scattering event, corresponding to either the deuterium or nuclear targets. During the run, the beam was offset from its ideal position, introducing sector-dependent effects in the vertex reconstruction. We used electron-proton elastic scattering to determine the beam offset and used this to correct the reconstructed interaction vertex for each event.

Once an event with a good electron was identified, we

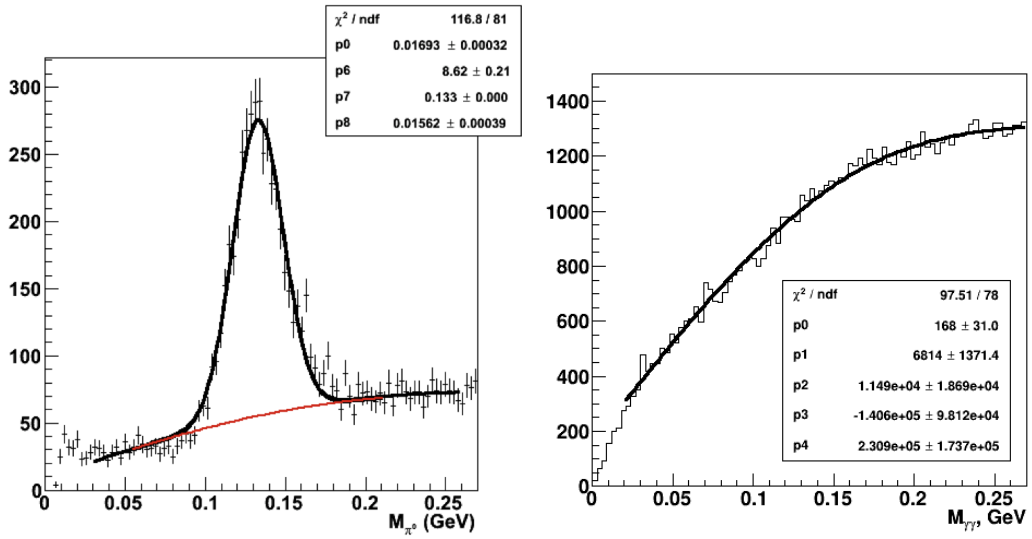

FIG. 1. Left: The number of events plotted versus the two-photon (π^0 candidate) invariant mass in a particular (ν, z, p_T^2) bin, showing the fit to a scaled mixed background (red) plus Gaussian. Right: The number of events plotted versus invariant mass for the corresponding mixed background fitted with a 4th order polynomial. The total signal plus background fit function is: $p[0]\cdot(p[1]+p[2]\cdot x+p[3]\cdot x^2+p[4]\cdot x^3+p[5]\cdot x^4)+p[6]\cdot\exp(\frac{-(x-p[7])^2}{2\cdot p[8]^2})$, where p_0 determines the background normalization, p_1-p_5 are fixed by the mixed-event fit, and p_6-p_8 are free parameters corresponding to the normalization, μ and σ of the Gaussian peak function. The fitting procedure was performed twice: first in the range $0.03 < M_{\gamma\gamma} < 0.25$ GeV to provide an estimate of μ and σ (corresponding to the notation of coefficients p[7] and p[8] of left plot), and then in the range (-5σ,+5σ) as indicated by the length of the red curve. The number of π^0 events is then calculated from the height of the Gaussian.

considered all the neutral hits in the EC with minimum uncorrected energy $E_\gamma > 0.3$ GeV. We separated photons from neutrons by cutting on the difference from the expected photon arrival time $\Delta t = t_{EC} - l_{EC}/30 - t_{start}$, where t_{EC} is the arrival time at the EC in ns, l_{EC} is the distance from the target to the EC hit in cm, the speed of light is 30 [cm/ns] and t_{start} is the event time at the target as determined from the electron [27]. To avoid transverse shower energy leakage, we rejected events at the edge of the EC. We rejected photons detected within 12° of the electron track to remove photons from bremsstrahlung radiation. We corrected the measured photon energy for a small momentum dependence of the EC sampling fraction to improve π^0 resolution [27]. We reconstructed π^0 candidates from all pairs of photons detected in each event and histogrammed the result as a function of π^0 invariant mass (see Fig. 1). After photon energy correction, the π^0 candidate minimum energy was $E_{\pi^0} > 0.5$ GeV.

Finally, to calculate the number of π^0's, the two-photon invariant mass spectrum was fit with a Gaussian peak function plus a polynomial background (see Fig. 1). Since the background in the two-photon invariant mass spectrum was combinatorial, we used an event mixing technique that consisted of combining photons from uncorrelated events. However, the resulting spectrum did not describe the backgrounds well. We therefore only combined photons from kinematically matched events. This new technique described the backgrounds well across all kinematics. A detailed description of the improved event-mixing technique can be found in [27]. We fit the resulting event-mixed background spectrum with a 4th-order polynomial. We then froze those parameters and fit the signal plus background spectrum with a constant times the background polynomial plus a three-parameter Gaussian. The number of π^0's was then calculated from the integral of the Gaussian function.

Corrections

The multiplicity ratio of Eq. 1 can be described as the super-ratio of the hadron number ratio for nucleus A and deuterium normalized by the electron number ratio for the same two nuclei. Corrections to the electron number ratio include: (i) acceptance correction factors due to electron acceptance in deuterium relative to the solid targets: these decrease the multiplicity ratio of a percent up to 8%; (ii) radiative corrections due to internal radiation: these increase the multiplicity ratio up to 3%; (iii) radiative corrections due to Coulomb distortion in the field of the nucleus: these decrease the multiplicity ratio by 0 to 4% with the largest corrections for Pb. Inclusive radiative corrections due to internal radiation are associated with bremsstrahlung off the nucleon from which the scattering took place and were calculated based on the Mo and Tsai formalism [28]. Calculation of the of the Coulomb corrections was based on the effective momen-

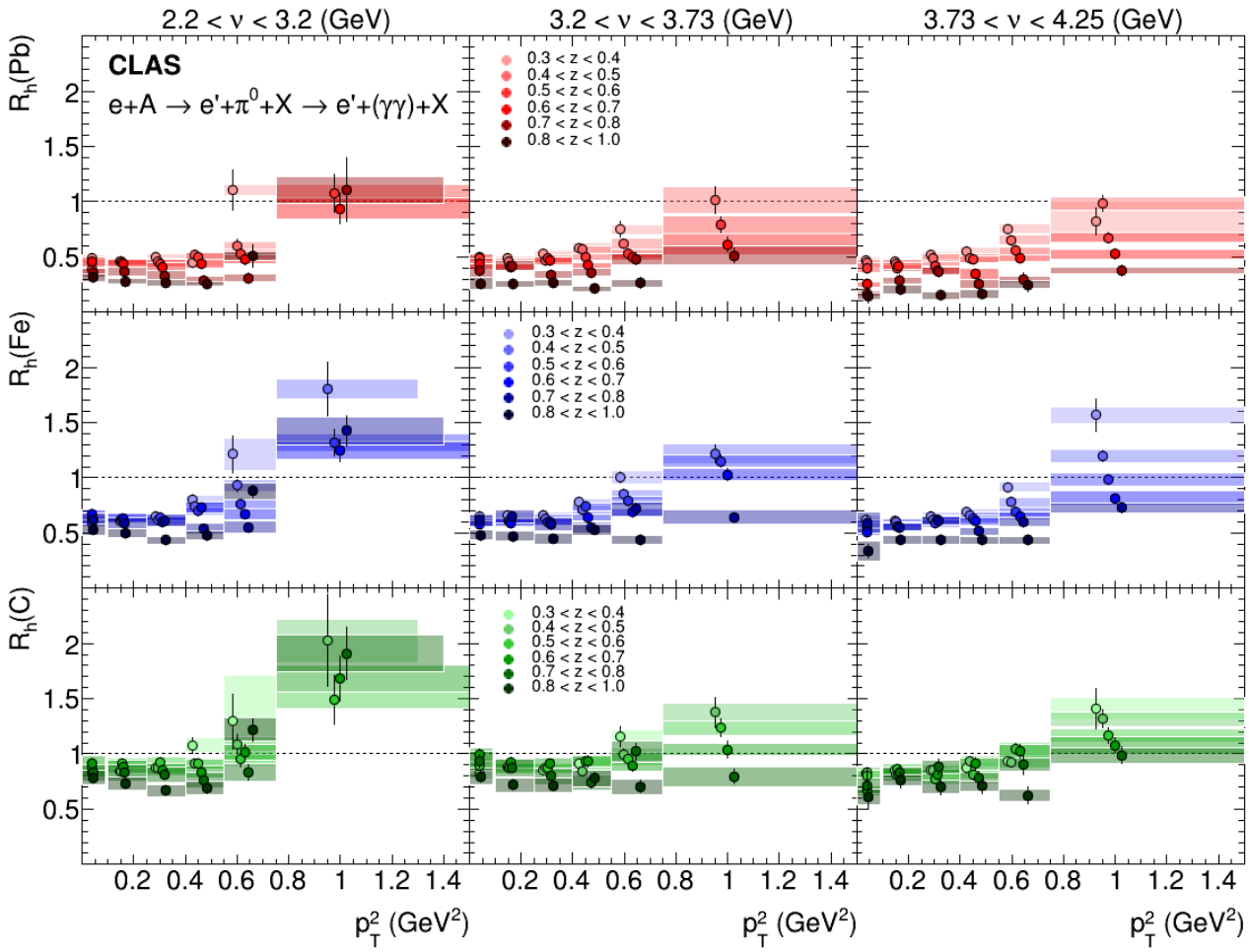

FIG. 2. π^0 multiplicity ratios for C, Fe, and Pb in (ν, z, p_T^2) bins plotted as a function of p_T^2 in bins of ν (top horizontal line) and z (indicated by the color). Points are shifted for ease of visualization around the mean value of p_T^2. Statistical uncertainties are indicated by black vertical lines; systematic uncertainties by the color bars. Horizontal uncertainties are related to the size of the bin: while for most bins in p_T^2 they are the same for each bin in z and target, a few bins have smaller uncertainty bands related to the interval of data significance in the bin.

tum approximation [29]. Both corrections are incorporated in the EXTERNAL code [30]. Additionally, there were radiative corrections due to external radiation, associated with bremsstrahlung in the target material; those were incorporated in the GEANT simulations and were accounted for by applying acceptance correction factors.

Corrections applied to the π^0 number ratio include: (i) acceptance correction factors, which change the multiplicity ratio depending on the binning: from -17% to +8% for (ν, z, p_T^2) bins and from -14% to +4% for (Q^2, ν, z) binning; (ii) radiative corrections for SIDIS π^0, which were calculated with the HAPRAD code [31] that was modified using empirically derived nuclear structure functions. These corrections affect the multiplicity ratio by less than 0.5%. The combined effect of radiative corrections on the multiplicity ratio from both the leptonic and hadronic number ratios does not exceed 4.8%. Finally, we calculated corrections due to the presence of the 15 μm aluminum entrance and exit walls (endcaps) of the liquid-deuterium target cell. The endcaps affect measurements of electrons and π^0 from the liquid-deuterium target. This correction decreased the multiplicity ratio by less than 1%.

We obtained acceptance correction factors by generating DIS events using the LEPTO 6.5.1 [32] Monte Carlo event generator, modified to include nuclear Fermi motion of the target nucleon according to the Ciofi-Simula parametrization [33]. The CLAS detector response was simulated with the GSIM package, based on GEANT3, which also includes the locations and materials of the

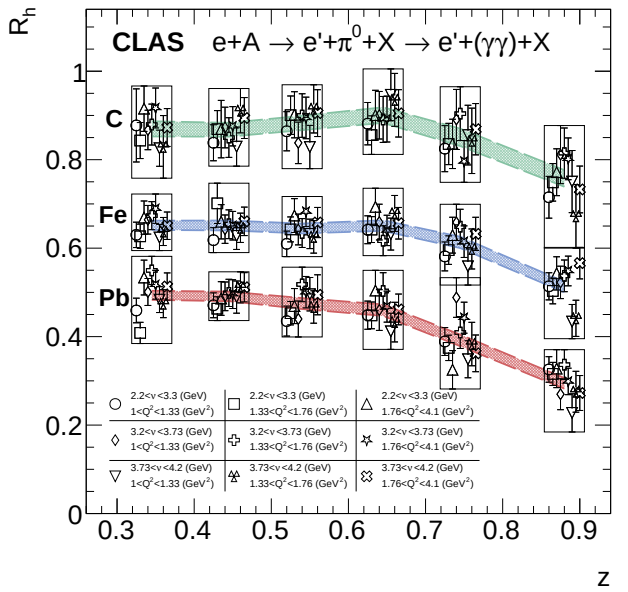

FIG. 3. π^0 multiplicity ratios for C, Fe, and Pb in (Q^2, ν, z) bins plotted as a function of z. Each one of the six bins in z contains 9 points corresponding to the 3 bins of ν and 3 bins in Q^2. Each of the 9 points in z is shifted around the center value of the bin; the points, plotted together with its statistical and systematic uncertainties, are enclosed in a box to improve the visualization. The center of the box is the center of the z bin, and the outermost uncertainty of each set defines the height of the box. Additionally, for the purpose of visualization, each target has a band drawn around the average with the width corresponding to the average of all measurements performed in each z-bin.

dual-target. Acceptance corrections were calculated on a bin-by-bin basis as the ratio of the number of generated events (electrons or π^0) to the number of reconstructed events per bin per target (solid or deuterium). Using simulations, we also removed a small number of bins that have significant bin migration effects, or, in other words, low purity.

The sources of systematic uncertainties include: (i) electron identification: target selection cuts, EC sampling fraction cuts, π^- contamination, DC fiducial cuts, and electron radiative corrections; (ii) photon identification: cut on minimum energy deposited in EC, time cut Δt, EC fiducial cuts; and (iii) π^0 identification: background and signal shapes of the invariant mass distribution, acceptance corrections, and SIDIS radiative corrections. Systematic uncertainties were evaluated independently for each set of bins, (ν, z, p_T^2) or (Q^2, ν, z), for each ratio of C, Fe, and Pb targets to D. They were then applied either as a normalization or as a bin-by-bin uncertainty. The largest contribution to the normalization-type uncertainty came from target vertex identification (target selection). It results in 3.1%, 2.4% and 2.3%, for C, Fe and and Pb, respectively, in the (ν, z, p_T^2) set of bins, and slightly smaller values for the (Q^2, ν, z) bins. The dominant source of the bin-by-bin systematic uncertainty is the π^0 invariant mass fit. This uncertainty includes both uncertainties on the background and signal shapes ranging on average from 1.4% for Fe in (Q^2, ν, z) bins to 4.7% for Pb in (ν, z, p_T^2) bins. The total average systematic uncertainties, including total normalization and bin-by-bin uncertainties in (Q^2, ν, z), are 5.0%, 4.9% and 6.9% for C, Fe and Pb multiplicities correspondingly; in (ν, z, p_T^2) they average to 7.1%, 7.1% and 9.6% for C, Fe and Pb, respectively. The average statistical uncertainty is typically several percent less.

RESULTS AND DISCUSSION

The measured three-fold multiplicity ratios of neutral pions in C, Fe and Pb are shown for bins of (ν, z) as a function of p_T^2 integrated over Q^2 (see Fig. 2) and for bins of (Q^2, ν) as a function of z integrated over p_T^2 (see Fig. 3). The data show increasing suppression for higher mass number corresponding to larger nuclei. The common trend for all three targets, as clearly observed in Fig. 3, is flat behavior of the multiplicity ratios in the range $0.3 < z < 0.65$ and monotonic decrease for higher z. The dependence on nuclear size indicates a path length-dependent process: for the smallest nucleus, carbon, suppression ranges from ∼10% to ∼25%, while for the largest nucleus, lead, the suppression ranges from 50% for moderate z reaching up to ∼75% at the highest z. From Fig. 3 we effectively observe no dependence on energy and momentum transfer to the system, *i.e* Q^2 and ν, in the range of our kinematics within the uncertainties of the measurement. However, our Q^2 and ν range is much less than that of HERMES.

Figure 2 shows the dependence of multiplicity ratio on p_T^2 in bins of z and ν. The global trend for all three targets is the enhancement of R_h at high p_T^2 and, again, an overall decrease with increasing z. R_h has a pronounced dependence on p_T^2 in correlation with z. The ratio is independent of p_T^2 for all values of z for $p_T^2 < 0.6$ GeV^2; it increases rapidly for large p_T^2 and small z to values that exceed unity. The largest enhancement of R_h is observed for the lightest nucleus, carbon, at the lowest ν bin, while the smallest enhancement is seen for lead at highest ν.

This suppression of neutral pions agrees quantitatively with the suppression observed in measurements of charged pions from the same CLAS dataset [34], and from previously published HERMES results [4, 7]. In modern versions of energy loss models [35], the overall attenuation as a function of z and the nuclear size is related to the assumption that the propagating quark emits multiple gluons and rescatters as it transverses the nuclear medium; the larger the nucleus, the more gluon emission

and quark energy loss it has. In the absorption types of models, for example, the color dipole model [8], the main source of hadron suppression is related to in-medium attenuation of the colorless pre-hadrons due to the length contraction of the propagating quark; this model also incorporates induced quark energy losses. In the framework of the GiBUU transport model [10], largely based on elastic and inelastic pre-hadronic final-state interactions, overall attenuation is understood in terms of pure hadron absorption due to increased interaction time with the nuclear medium.

The pattern of p_T^2 enhancement at low z and high p_T^2, observed in Fig. 2, is often referred to as a type of Cronin effect [36]. It was first observed in the measurements by EMC [37], later by FNAL [38], and further confirmed by HERMES [7]. This behavior is qualitatively similar to the previous measurements, however, in contrast to the published CLAS and HERMES results on charged pions, we observe the largest enhancement at high p_T^2 for lightest nucleus - carbon, and the lowest enhancement for the heaviest nucleus - lead. Such nuclear ordering of the Cronin effect qualitatively reminiscent of enhancement of di-hadron pairs at large di-pion invariant mass [39]. Cronin effect shows a modest dependence on ν, which is more pronounced for heavier nuclei compared to the lighter one.

Theoretically, the Cronin effect has been explained in terms of multiple parton scattering prior to its fragmentation. In the limit $z \to 1$, the lifetime of the propagating quark vanishes as it is not allowed to lose any energy and, thus, cannot accumulate transverse momentum through re-scattering. On the other hand, the low z regime pertains to the opposite behavior that leads to the enhancement of transverse momenta. Such a scenario also suggests that the attenuation in the limit $z \to 1$ is purely due to hadron absorption. The dependence of the Cronin effect on the nuclear size points to a competition between partonic multiple scattering, which causes enhancement, and hadronic inelastic scattering, which causes suppression.

CONCLUSIONS

In this paper we presented the first differential π^0 multiplicity ratios produced in SIDIS off D, C, Fe and Pb with a 5.014 GeV electron beam and measured with the CLAS detector. The results were reported in two sets of bins: $R_{\rm h}(\nu,\, z,\, p_T^2)$ and $R_{\rm h}(Q^2,\, \nu,\, z)$. As expected, the data show a larger suppression of $R_{\rm h}$ for higher atomic number. The suppression is constant for moderate z and then decreases rapidly for leading hadrons ($z > 0.65$); the maximum suppression varies from 25% on carbon to 75% on lead. The multiplicity ratio $R_{\rm h}$ is enhanced for large p_T^2 and small z. This enhancement is the largest for carbon and the smallest for lead. Such behavior is opposite to the published HERMES results, which suggests a competition between partonic multiple scattering, which causes enhancement, and hadronic inelastic scattering, which causes suppression. Both effects, suppression and enhancement of multiplicity ratios, are largely independent of Q^2, while the Cronin effect shows a modest dependence on ν.

These data, once explored in the framework of existing theoretical models, will provide detailed information on the dynamics of partonic multiple scattering and in-medium hadron interactions, allowing for better characterization of their relative contributions. These measurements will be extended in the near future with an 11 GeV electron beam in the approved Jefferson Lab experiment E12-06-117 [40]. Offering a wider range in Q^2 and ν and higher luminosity, a wealth of new physics will be available, for example: access to the quark mass dependence of the hadronization with GeV-scale meson formation, extraction of four-fold multiplicities for a large spectrum of hadrons, and searches for di-quark correlations in baryon formation [41]. With its collider energies and largely extended range in kinematical variables, the proposed eA program at the EIC [42] will access completely new information on hadronization mechanisms, such as, clean measurements of medium induced energy loss in the regime where hadrons are formed outside the nuclear medium and studies of potentially very different hadronization properties of heavy mesons.

We acknowledge the outstanding efforts of the staff of the Accelerator and the Physics Divisions at Jefferson Lab in making this experiment possible. This work is supported by the Chilean Agencia Nacional de Investigacion y Desarollo (ANID), FONDECYT grants No.11181215 and No.1221827, No.1161642 and No.1201964, ANID PIA/APOYO AFB180002, and by the ANID-Millennium. Science Initiative Program - ICN2019_044. The Southeastern Universities Research Association (SURA) operates the Thomas Jefferson National Accelerator Facility for the U.S. Department of Energy under Contract No. DE-AC05-06OR23177.

* taisiya.mineeva@usm.cl

[1] V. Del Duca, S. J. Brodsky, and P. Hoyer, Phys. Rev. D **46**, 931 (1992).
[2] A. Airapetian, H. Bulten, W. Hesselink, A. Laziev, J. Martin, F. Schmidt, M. Simani, E. Thomas, J. van den Brand, and J. de Visser, European Physical Journal C. Particles and Fields **20**, 479 (2001).
[3] A. Airapetian *et al.* (HERMES Collaboration), Physics Letters B **577**, 37 (2003).
[4] A. Airapetian *et al.* (HERMES Collaboration), Nucl. Phys. B **780**, 1 (2007), arXiv:0704.3270 [hep-ex].
[5] A. Airapetian *et al.* (HERMES Collaboration), Phys. Rev. Lett. **96**, 162301 (2006), arXiv:hep-ex/0510030.
[6] A. Airapetian *et al.* (HERMES Collaboration), Phys.

Lett. B **684**, 114 (2010), arXiv:0906.2478 [hep-ex].

[7] A. Airapetian *et al.* (HERMES Collaboration), Eur. Phys. J. A **47**, 113 (2011), arXiv:1107.3496 [hep-ex].

[8] B. Kopeliovich, J. Nemchik, E. Predazzi, and A. Hayashigaki, Nuclear Physics A **740**, 211–245 (2004).

[9] B. Guiot and B. Z. Kopeliovich, Physical Review C **102** (2020), 10.1103/physrevc.102.045201.

[10] K. Gallmeister and U. Mosel, Nuclear Physics A **801**, 68–79 (2008).

[11] T. Falter, W. Cassing, K. Gallmeister, and U. Mosel, Acta Physica Hungarica A) Heavy Ion Physics **27**, 71–78 (2006).

[12] T. Falter, W. Cassing, K. Gallmeister, and U. Mosel, Physical Review C **70** (2004), 10.1103/physrevc.70.054609.

[13] T. Falter and U. Mosel, Fizika B **13**, 165 (2004), arXiv:nucl-th/0308073.

[14] T. Falter, W. Cassing, K. Gallmeister, and U. Mosel, Physics Letters B **594**, 61–68 (2004).

[15] X.-N. Wang, Nuclear Physics A **702**, 238–248 (2002).

[16] J. Osborne and X.-N. Wang, Nuclear Physics A **710**, 281–302 (2002).

[17] N.-B. Chang, W.-T. Deng, and X.-N. Wang, Physical Review C **89** (2014), 10.1103/physrevc.89.034911.

[18] A. Majumder, E. Wang, and X.-N. Wang, Phys. Rev. Lett. **99**, 152301 (2007).

[19] B.-W. Zhang, X.-N. Wang, and A. Schäfer, Nuclear Physics A **783**, 551–554 (2007).

[20] X.-N. Wang, Nuclear Physics A **702**, 238–248 (2002).

[21] Z.-B. Kang, E. Wang, X.-N. Wang, and H. Xing, Physical Review D **94** (2016), 10.1103/physrevd.94.114024.

[22] W. K. Brooks and J. A. López, Physics Letters B **816**, 136171 (2021).

[23] B. Z. Kopeliovich, H.-J. Pirner, I. K. Potashnikova, I. Schmidt, A. V. Tarasov, and O. O. Voskresenskaya, Physical Review C **78** (2008), 10.1103/physrevc.78.055204.

[24] A. Accardi, F. Arleo, W. K. Brooks, D. D'enterria, and V. Muccifora, La Rivista del Nuovo Cimento **32**, 439–554 (2009).

[25] B. A. Mecking *et al.*, Nucl. Instrum. Meth. A **503**, 513 (2003).

[26] H. Hakobyan *et al.*, Nuclear Instruments and Methods in Physics Research Section A: Accelerators, Spectrometers, Detectors and Associated Equipment **592**, 218 (2008).

[27] T. Mineeva, *Hadronization Studies via Electroproduction off D, C, Fe, and Pb*, Ph.D. thesis, University of Connecticut (2013).

[28] L. W. Mo and Y. S. Tsai, Rev. Mod. Phys. **41**, 205 (1969).

[29] A. Aste, C. von Arx, and D. Trautmann, The European Physical Journal A **26**, 167 (2005).

[30] S. Dasu, P. De Barbaro, A. Bodek, H. Harada, M. Krasny, K. Lang, E. Riordan, L. Andivahis, R. Arnold, D. Benton, *et al.*, Physical Review D **49**, 5641 (1994).

[31] I. Akushevich, N. Shumeiko, and A. Soroko, Eur. Phys. J. C **10**, 681 (1999).

[32] G. Ingelman, A. Edin, and J. Rathsman, Computer Physics Communications **101**, 108 (1997).

[33] C. Ciofi degli Atti and S. Simula, Phys. Rev. C **53**, 1689 (1996).

[34] S. Moran *et al.* (CLAS), Phys. Rev. C **105**, 015201 (2022), arXiv:2109.09951 [nucl-ex].

[35] A. Majumder and M. Van Leeuwen, Prog. Part. Nucl. Phys. **66**, 41 (2011), arXiv:1002.2206 [hep-ph].

[36] J. W. Cronin, H. J. Frisch, M. J. Shochet, J. P. Boymond, P. A. Piroue, and R. L. Sumner, Phys. Rev. D **11**, 3105 (1975).

[37] J. Ashman *et al.* (European Muon Collaboration), Z. Phys. C **52**, 1 (1991).

[38] M. R. Adams *et al.* (E665), Phys. Rev. Lett. **74**, 5198 (1995), [Erratum: Phys.Rev.Lett. 80, 2020–2021 (1998)].

[39] S. Paul *et al.*, **129** (2022), 10.1103/physrevlett.129.182501.

[40] W. K. Brooks *et al.*, "Quark propagation and hadron formation," `https://www.jlab.org/exp_prog/proposals/10/PR12-06-117.pdf` (2010), a CLAS Collaboration proposal.

[41] M. Barabanov *et al.*, Progress in Particle and Nuclear Physics (2021), https://doi.org/10.1016/j.ppnp.2020.103835.

[42] R. A. Khalek *et al.*, "Science Requirements and Detector Concepts for the Electron-Ion Collider: EIC Yellow Report," (2021), arXiv:2103.05419 [physics.ins-det].